Cryogenic NMR spectroscopy of endohedral hydrogen-fullerene complexes

AUTHOR(S):

Carravetta, M; Johannessen, OG; Levitt, MH; Heinmaa, I; Stern, R; Samoson, A; Horsewill, AJ; Murata, Y; Komatsu, K

CITATION:

Carravetta, M ...[et al]. Cryogenic NMR spectroscopy of endohedral hydrogen-fullerene complexes. JOURNAL OF CHEMICAL PHYSICS 2006, 124(10): 104507.

ISSUE DATE:

2006-03-14

URL:

http://hdl.handle.net/2433/39769

THE JOURNAL OF CHEMICAL PHYSICS **124**, 104507 (2006)

Cryogenic NMR spectroscopy of endohedral hydrogen-fullerene complexes

M. Carravetta, O. G. Johannessen, and M. H. Levitt[a)]
School of Chemistry, Southampton University, Southampton SO17 1BJ, United Kingdom

I. Heinmaa, R. Stern, and A. Samoson
National Institute of Chemical Physics and Biophysics, 12618 Tallinn, Estonia

A. J. Horsewill
School of Physics and Astronomy, University of Nottingham, Nottingham NG7 2RD, United Kingdom

Y. Murata and K. Komatsu
Institute for Chemical Research, Kyoto University, Kyoto 611-0011, Japan

(Received 8 November 2005; accepted 19 January 2006; published online 13 March 2006)

We have observed ^{1}H NMR spectra of hydrogen molecules trapped inside modified fullerene cages under cryogenic conditions. Experiments on static samples were performed at sample temperatures down to 4.3 K, while magic-angle-spinning (MAS) experiments were performed at temperatures down to 20 K at spinning frequencies of 15 kHz. Both types of NMR spectra show a large increase in the intramolecular ^{1}H–^{1}H dipolar coupling at temperatures below 50 K, revealing thermal selection of a small number of spatial rotational states. The static and MAS spectra were compared to estimate the degree of sample heating in high-speed cryogenic MAS-NMR experiments. The cryogenic MAS-NMR data show that the site resolution of magic-angle-spinning NMR may be combined with the high signal strength of cryogenic operation and that cryogenic phenomena may be studied with chemical site selectivity. © *2006 American Institute of Physics*.
[DOI: 10.1063/1.2174012]

I. INTRODUCTION

Many examples of insertion of individual atoms inside fullerene derivatives using forced conditions are available.[1–5] Several research groups have synthesized remarkable chemical complexes, in which the molecular cage of a fullerene (C_{60}) derivative encloses a molecule of hydrogen (H_2).[6–9] Particularly high yields have been achieved for the endohedral complex of hydrogen H_2 and aza-thia-open-cage-fullerene (ATOCF),[7,10] whose structure is shown in Fig. 1. In this article, we report ^{1}H NMR data of H_2@ATOCF, taken at cryogenic temperatures (down to 4.3 K). These data illustrate the rotational quantization of the endohedral H_2 molecules at low temperatures, and suggest applications of these endohedral complexes as cryogenic NMR thermometers, and as cryogenic relaxation enhancement agents.

In an earlier publication,[11] we reported double-quantum magic-angle-spinning (MAS) NMR experiments on H_2@ATOCF at temperatures down to around 100 K. The ^{1}H NMR peaks of the endohedral H_2 molecules could readily be resolved by using MAS, and the double-quantum data showed that the rotational motion of the H_2 molecules was fast and almost isotropic, with an order parameter around 2%, increasing slightly as the temperature was reduced. We also showed that at slow MAS frequencies, the H_2 protons are in thermal contact with the ^{1}H nuclei on the exterior of the fullerene cage, so that all protons in the sample relax with a common time constant. We found that magic-angle spinning faster than around 15 kHz breaks this thermal contact, so that the endohedral and exohedral protons behave as independent spin order reservoirs, with very different relaxation rate constants.

We now explore the behavior of the endohedral H_2 protons at cryogenic temperatures ($\lesssim$50 K). This is of great interest for several reasons. First, the rotational energy level splitting of gas-phase H_2 is of the order of 50 K in temperature units. The behavior of the H_2 molecules is expected to change dramatically below this temperature, since only a small number of rotational quantum states should be populated. Second, one expects the endohedral hydrogen molecules to enjoy extreme rotational freedom, even in the cryogenic regime, where most molecular motions start to freeze out. Since spin-lattice relaxation is driven by molecular motion, rapid spin relaxation is expected for the H_2 protons even under cryogenic conditions.

MAS-NMR allows one to achieve chemical site resolution in the solid state, providing that the spinning frequency is high enough.[12,13] Since H_2@ATOCF contains both endohedral and exohedral protons, it is very desirable to conduct cryogenic NMR experiments under MAS conditions. However, early demonstrations of cryogenic MAS-NMR could only achieve slow spinning frequencies of around 1 kHz[14,15]—usually not enough to resolve distinct ^{1}H resonances. Fortunately, technical developments have now made it possible to perform cryogenic MAS-NMR experiments at spinning frequencies up to around 20 kHz.[16] It is therefore possible to explore cryogenic phenomena such as rotational state selection, while retaining chemical site selectivity. This is illustrated in Fig. 1, which shows a series of ^{1}H NMR spectra, taken at temperatures in the range of 16.2–279 K, at

a)Electronic mail: mhl@soton.ac.uk

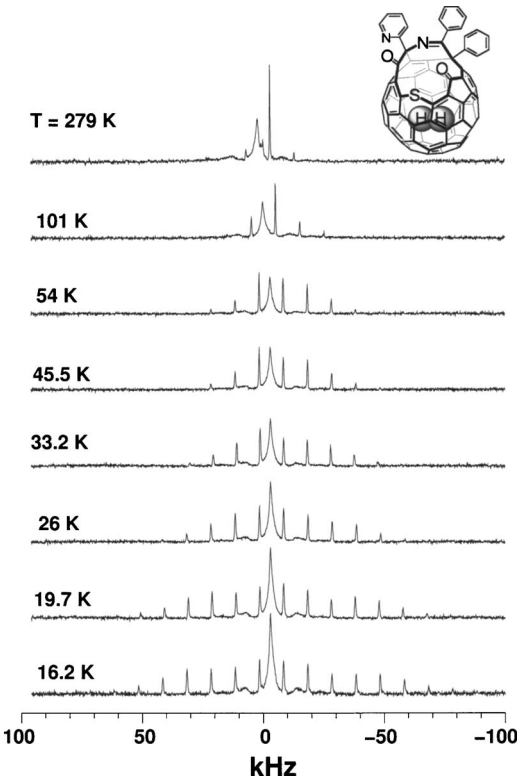

FIG. 1. MAS ^{1}H spectra of H_2@ATOCF (inset) as a function of temperature. All experiments were recorded at a spinning frequency $\omega_r/2\pi = 10.0$ kHz and a field of 8.46 T, using a spin echo sequence of duration $\tau = 100$ μs to suppress the exohedral ^{1}H signal.

a MAS frequency of 10.00±0.05 kHz. All spectra display a broad spectral feature from the immobile exohedral protons on the aromatic rings attached to the fullerene cage, and a set of narrow sidebands from the highly mobile endohedral H_2 protons (as discussed below, the exohedral signals were partially suppressed by using a spin echo method). In the case of the 279 K spectrum, the spinning sidebands from the endohedral protons are small. These sidebands are due to the dipole-dipole coupling between the H_2 protons, which is averaged to a small residual value by the rapid, nearly isotropic, molecular motion. The small residual dipolar coupling is periodically modulated by the magic-angle sample rotation, giving rise to spinning sidebands. As the sample is cooled, the number of sidebands increases rapidly, indicating that the H_2 rotation becomes increasingly anisotropic at low temperatures. We argue below that the spectra at the lowest temperatures are best described by taking into account the quantized spatial rotational states of the H_2 molecules, rather than by using the semiclassical concept of motional averaging. Figure 1 therefore illustrates the use of cryogenic MAS-NMR for investigating cryogenic quantum phenomena with chemical site selectivity.

II. EXPERIMENT

A. Sample preparation

The sample is an endohedral 1:1 complex of molecular hydrogen and ATOCF, referred to as H_2@ATOCF, shown in the inset of Fig. 1. It was prepared in high purity using a published procedure[7,10] and is stable under ordinary conditions.

B. NMR measurements

The NMR measurements were performed both in a relatively high magnetic field (8.46 T, corresponding to a proton Larmor frequency of 360 MHz) and in a low magnetic field (0.735 T, corresponding to a proton Larmor frequency of 31.5 MHz).

1. High-field NMR *measurements*

The 8.46 T NMR equipment (Tallinn, Estonia) has both static and MAS-NMR capabilities at cryogenic sample temperatures[16] and allows Fourier transformation of the free-induction decays in order to obtain spectral information.

The cryogenic MAS experiments were performed using a homebuilt probe mounted in a 70 mm outer-diameter He-flow cryostat (Janis Research Co.). The NMR probe was inserted into the 89 mm bore 8.46 T superconducting NMR magnet from the top. A 6.5 mg sample of H_2@ATOCF was loaded into a homebuilt ZrO_2 rotor with an outer diameter of 1.8 mm. The radio frequency fields used provided a ^{1}H nutation frequency of around 150 kHz. The sample was rotated at frequencies up to 20 kHz using He drive and bearing gas. Temperature control down to 15 K was achieved by varying the boiloff rate of a liquid He reservoir in the base of the NMR probe. The sample temperature was monitored by a sensor (calibrated LakeShore Cernox) mounted into a copper plate exposed to the exit gas stream, around 20 mm from the sample. To obtain temperatures below 30 K, the He drive gas was cooled by a liquid-N_2 heat exchanger, before it entered the probe. The MAS experiments typically required ~ 2 dm^3 h^{-1} liquid He and ~ 2 m^3 h^{-1} He gas. All He were recovered and recycled. Technical details of the cryogenic MAS probe will be reported elsewhere.

The high-field static NMR experiments were performed on a second homebuilt cryogenic NMR probe, using a solenoid rf coil perpendicular to the static field. The sample temperature could be controlled with an accuracy of ±0.1 K down to 4.3 K.

2. Low-field (NMR) *measurements*

The 0.735 T NMR equipment (Nottingham, UK) is designed for spin-lattice relaxation time constant (T_1) measurements as a function of temperature and magnetic field.[17] The NMR probe uses a helium-flow cryostat providing sample temperature control with a stability of ±0.05 K, as detected by a calibrated LakeShore Cernox sensor. The low-field ^{1}H T_1 measurements were performed on 25 mg of H_2@ATOCF, placed in a 5 mm glass NMR tube. The T_1 measurement was made by measuring the recovery curve of the integrated signal intensity after radio frequency saturation. The saturation-recovery curve was sampled with equal increments in the logarithm of time between approximately 0.01 times T_1 and 30 times T_1. Some of the recovery curves displayed a slight nonexponentiality, which was ignored in the analysis.

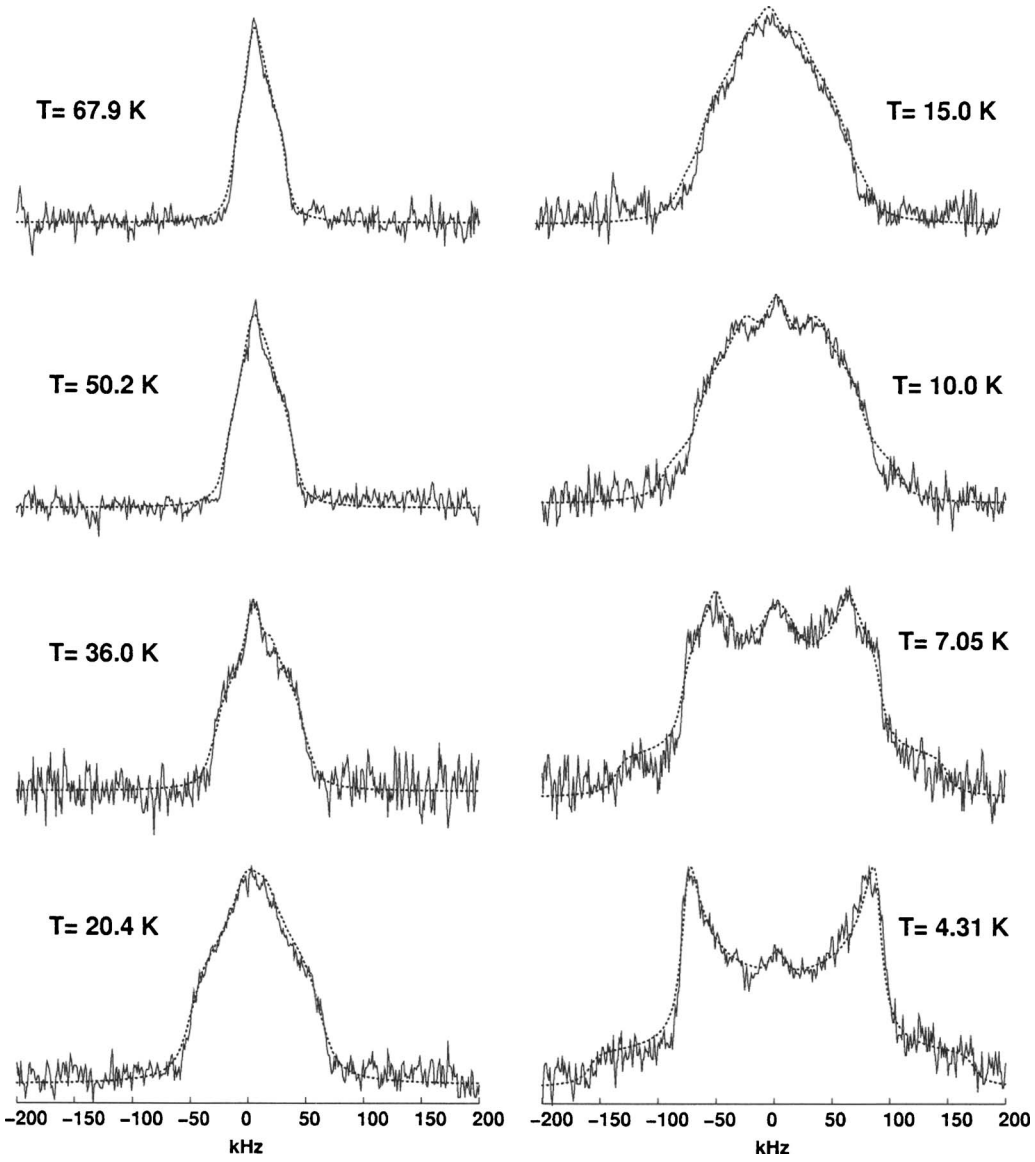

FIG. 2. Solid lines: static ^{1}H spectra of H_2@ATOCF as a function of temperature, recorded with a $(\pi/2)_x-\tau/2-(\pi/2)_y-\tau/2$ solid echo sequence of duration τ=400 μs at a field of 8.46 T. Dotted lines: best fit simulations using a temperature-dependent biaxial dipole-dipole coupling (see Fig. 8).

C. Numerical simulations

All numerical simulations of NMR line shapes were performed using the GAMMA computational platform,[29] version 4.0.5B. Analysis of experimental NMR data was performed using the MATNMR software package.[33]

III. RESULTS

A. Static NMR spectra

In the absence of MAS, the ^{1}H spectra of H_2@ATOCF are dominated by a broad, featureless signal from the exohedral protons of the aromatic groups attached to the orifice, which outnumber the endohedral protons by a ratio of 8:1. In order to observe the endohedral proton signal, we used a "solid echo" pulse sequence $(\pi/2)_x-\tau/2-(\pi/2)_y-\tau/2-$(detect). The NMR signals of the endohedral H_2 protons comprise accurate spin echoes under the solid echo pulse sequence, since the H_2 nuclei form approximately isolated spin-1/2 pairs. The exohedral protons, on the other hand, participate in a complex multiple-spin coupling network, for which the solid echo sequence is largely ineffective.

Figure 2 shows a series of solid echo NMR spectra of a static sample of H_2@ATOCF, obtained at a magnetic field of 8.46 T and a variety of temperatures, using a solid echo with τ=400 μs. As the sample is cooled below 20 K, the powder line shapes broaden significantly. At 4.31 K, the proton spectrum takes the form of a classic Pake pattern (except for a small central feature, attributed to a residual exohedral signal). There are pronounced deviations from the classic Pake line shape at 7.05 K and above.

The integrated intensity of the experimental NMR signals is plotted against the temperature in Fig. 3. The observed linear dependence indicates normal Curie paramagnetism of the nuclear spin system. There is no evidence of anomalies due to *ortho-para* interconversion on the time scale of the experiment, which lasted around 12 h (see below).

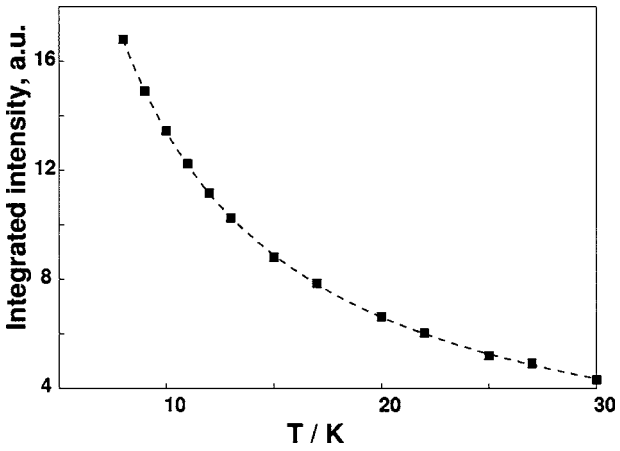

FIG. 3. Signal intensity vs temperature T, as determined from static spectra at a field of 0.735 T. The behavior is consistent with the Curie law, indicating no evidence of *ortho-para* interconversion.

B. Cryogenic MAS NMR spectra

The set of cryogenic MAS spectra shown in Fig. 1 was obtained at $\omega_r/2\pi=10.0$ kHz using a spin echo pulse sequence of the form $(\pi/2)_x-\tau/2-\pi_y-\tau/2-$(detect) with a spin echo duration of $\tau=200$ μs. The spin echo sequence produced partial suppression of the broad exohedral proton signal. However, the sideband amplitudes were found to fluctuate strongly in this experiment, presumably because the synchronization between the echo pulse and the sample rotation is perturbed by instabilities in the spinning frequency at cryogenic temperatures.

In order to obtain more reproducible data, we also performed MAS-NMR experiments at a spinning frequency $|\omega_r/2\pi|=15.0\pm0.2$ kHz using a single $\pi/2$ pulse for the excitation of transverse magnetization. NMR spectra are shown in the left column of Fig. 4 for a variety of temperatures. Each of these spectra was produced by collecting several single transients, and Fourier transforming them individually. A linear superposition of the single-transient spectra was computed, using the spinning sideband pattern to estimate the spinning frequency for each transient. Each spectrum was scaled slightly along the horizontal axis to correct for the small variations in the spinning frequency. Figure 4 (left column) shows the narrow spinning sidebands from the endohedral H_2 molecules superposed on the strong broad signal from the exohedral protons.

C. Spin-lattice relaxation

The ^{1}H spin-lattice relaxation time T_1 was measured as a function of temperature at magnetic fields of 0.735 and 8.46 T, using a standard inversion-recovery pulse sequence on a static sample. The T_1 of the endohedral ^{1}H peak was also measured in the presence of 18 kHz MAS at a field of 8.46 T. The results are shown in Fig. 5. All curves have the same general shape, with an obvious T_1 minimum at a temperature of around 60 K. The relaxation of static samples is faster at a field of 0.735 T compared to 8.46 T. Magic-angle spinning speeds up the spin-lattice relaxation of the endohedral protons by around an order of magnitude. This effect may be attributed to a breaking of the thermal contact between the fast-relaxing endohedral protons and the slowly relaxing exohedral protons at high MAS frequencies, as discussed before.[11] The minimum observed T_1 is around 12 ms at 65 K, in the presence of MAS.

The ^{1}H T_1 of static H_2@ATOCF samples is plotted against inverse temperature T^{-1} in Fig. 6, in order to emphasize the cryogenic behavior. At both fields there is a roughly linear dependence of T_1 on T^{-1} in the cryogenic regime below 50 K.

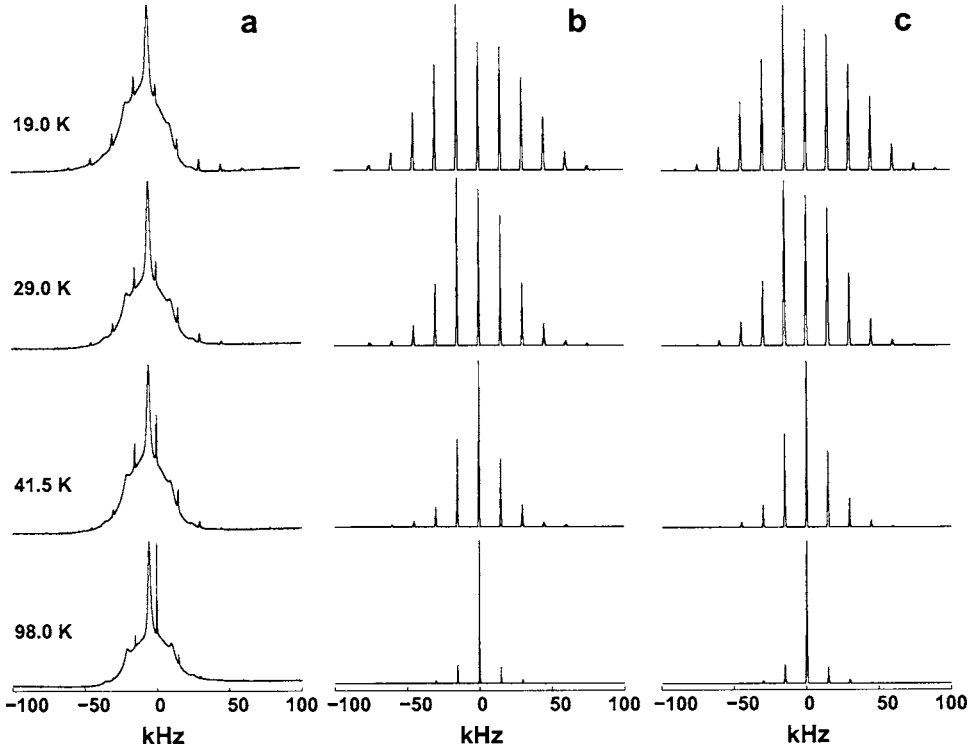

FIG. 4. (a) Magic-angle-spinning ^{1}H spectra of H_2@ATOCF as function of temperature, using single-pulse excitation at a field of 8.46 T. The broad feature and the narrow spinning sidebands are from the exohedral and endohedral protons, respectively. (b) Estimates of the endohedral spinning sideband amplitudes. (c) Best fits of the spinning sideband amplitudes to simulations using a temperature-dependent biaxial dipole-dipole coupling (see Fig. 8) and a chemical shift anisotropy interaction. The chemical shift anisotropy interaction was fixed at $\delta^{CSA}=8.3$ ppm and $\eta^{CSA}=0$, with the same principal axis system as the DD interaction.

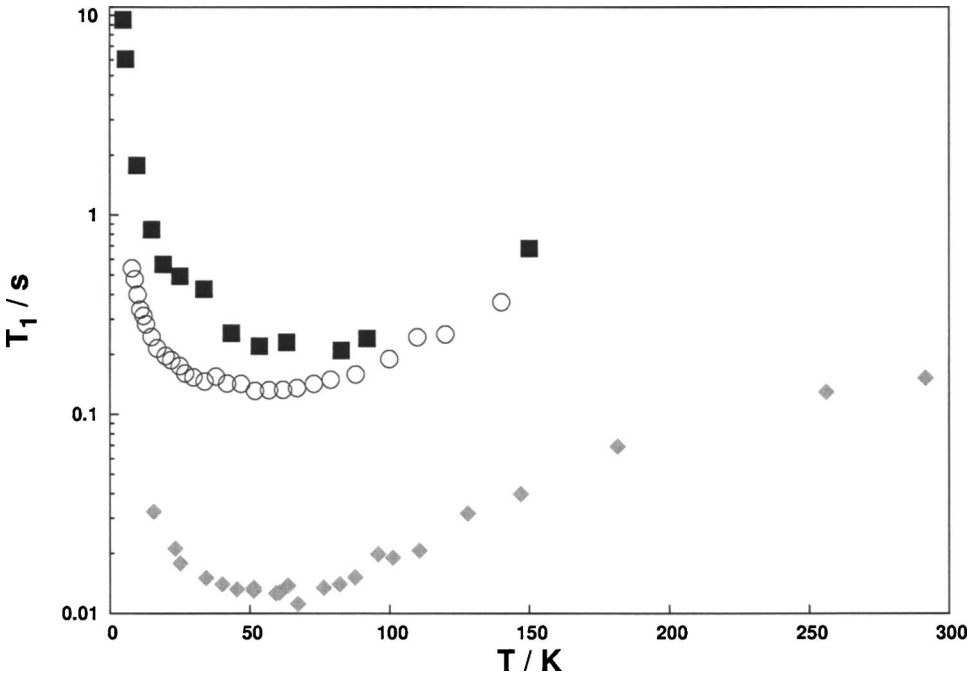

FIG. 5. ^{1}H spin-lattice relaxation time constants T_1 for H_2@ATOCF as a function of temperature T. Black squares: T_1 of a static sample, in a magnetic field of 8.46 T Grey diamonds: T_1 of a static sample, in a magnetic field of 0.735 T. Circles: T_1 of a magic-angle-spinning sample (spinning frequency=18 kHz), in a magnetic field of 8.46 T.

IV. DISCUSSION

A. Energy level structure

A hydrogen molecule trapped inside a fullerene cage is a very interesting system from a quantum-mechanical point of view. The H_2 molecule has internal rotational and vibrational degrees of freedom. In addition, the H_2 molecule behaves as a particle trapped in a three-dimensional box, and displays translational quantization. Furthermore, the nuclear spin states are entangled with the rotational states, due to the requirements of the Pauli principle.

Confined hydrogen molecules have been studied in a variety of contexts by NMR,[18–21] including H_2 molecules trapped in the interstices of a fullerene lattice.[22] The system studied here is unique because of its chemical and physical stabilities, allowing study under a wide variety of conditions including magic-angle spinning.

A hydrogen molecule trapped inside the fullerene cavity has six spatial degrees of freedom—three translational, two rotational, and one vibrational—as well as the nuclear spin degrees of freedom. In the following discussion, the endohedral H_2 molecules are assumed to be in the ground vibrational state (v=0) over the experimental temperature range, since the vibrational splitting is $\hbar\omega_{\mathrm{vib}}/k_B \cong 5950$ K,[23] close to that expected for free hydrogen gas. The spatial state of a confined H_2 molecule may therefore be indexed by five quantum numbers, and is denoted $|Jm_J n \ell m_\ell\rangle$, where $\{J, m_J\}$

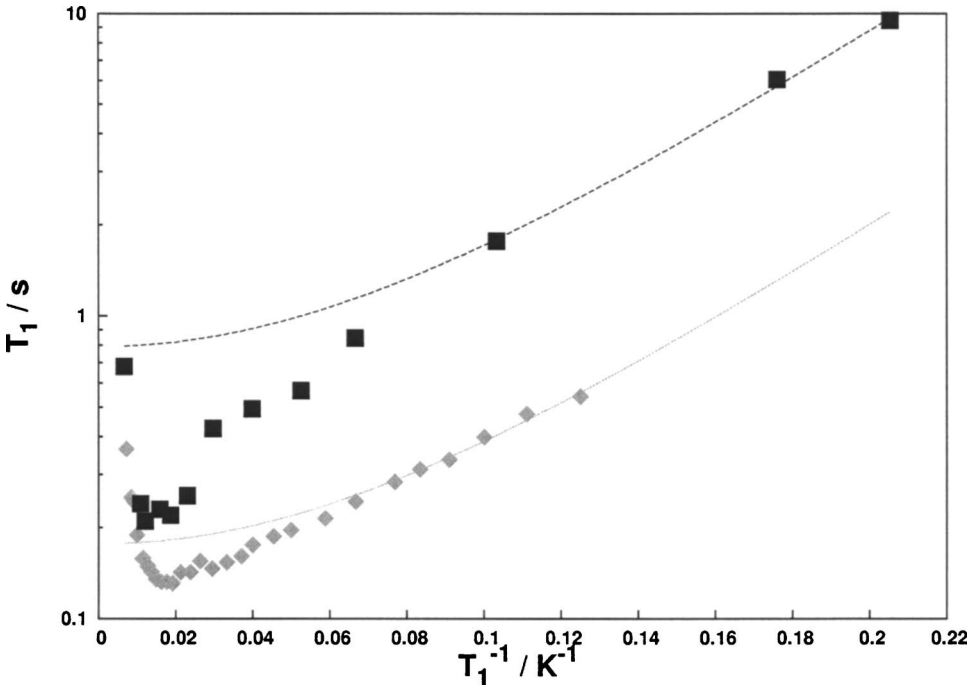

FIG. 6. ^{1}H spin-lattice relaxation time constants T_1 for H_2@ATOCF as a function of inverse temperature T^{-1}. Black squares: T_1 of a static sample, in a magnetic field of 8.46 T. Grey diamonds: T_1 of a static sample, in a magnetic field of 0.735 T. Solid line: best fit of the 0.735 T data to Eq. (27), using $\Delta E_{\mathrm{LL}}/k_B = 18.8 \pm 0.7$ K. Dashed line: best fit of the 8.46 T data to Eq. (27), using $\Delta E_{\mathrm{LL}}/k_B = 18.6 \pm 2.1$ K.

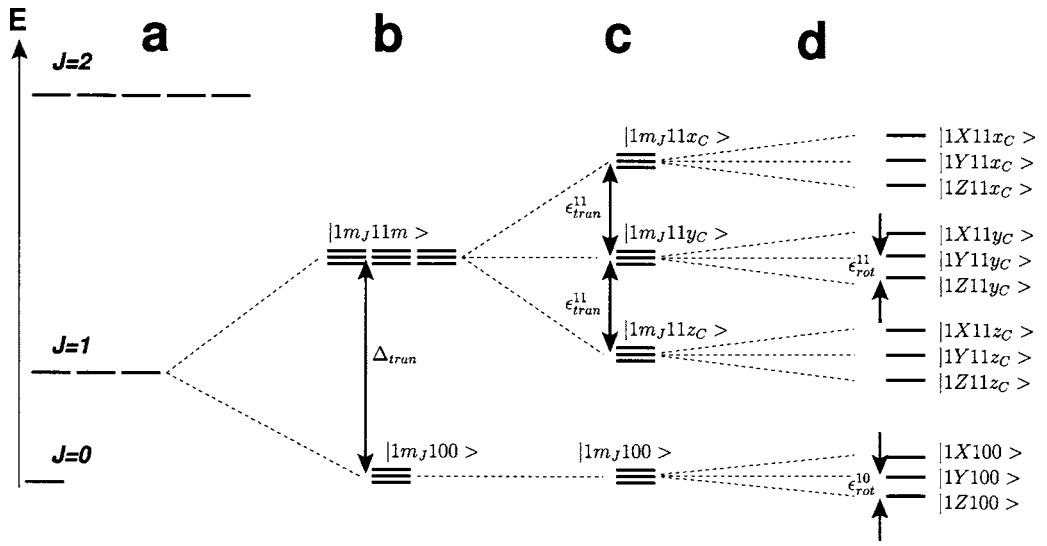

FIG. 7. Hypothetical rototranslational energy level diagram for molecular hydrogen inside ATOCF cavity. (a) Rotational energy levels and rotational degeneracies of a free H_2 rotor. (b) Splitting of the $J=1$ rotational state due to translational quantization in a spherical box. Only the two lowest levels are shown. The states are labeled $|Jm_jn\ell m\rangle$, where m_j is the rotational sublevel quantum number and $\{n,\ell,m\}$ are translational quantum numbers. The total degeneracies (both translational and rotational) are displayed. (c) Splitting of the translational excited state due to cavity elongation. The translational excited state levels are labelled $|1m_j11\mu_C\rangle$, where $\mu_C\in\{x_C,y_C,z_C\}$ to indicate quenching of orbital angular momentum and translational polarization along the cavity axis system. (d) Splitting of each translational state due to a nonisotropic rotational potential. The energy levels are labelled $|J\mu_jn\ell\mu_C\rangle$ with $\mu_J\in\{X,Y,Z\}$ to indicate quenching of rotational angular momentum and rotational polarization along the principal axis system of the rotational potential.

are the rotational quantum numbers and $\{n,\ell,m_\ell\}$ are the translational quantum numbers. The postulated energy level structure of the endohedral H_2 molecules is sketched in Fig. 7.

1. Rotational quantization

The rotational levels of the confined H_2 molecules are expected to resemble those in hydrogen gas, which are given by

$$E_J = B_J J(J+1), \tag{1}$$

where B_J is the rotational constant, given by $B_J/k_B=86$ K in the free gas. The lowest three rotational levels are sketched in Fig. 7(a). At the temperatures used in the experiments, the $J=3$ level is assumed to be unpopulated.

Since the H_2 nuclei are identical fermions, the Pauli principle requires that the nuclear spin states of the even-J molecules (parahydrogen) are antisymmetric with respect to particle exchange, while the nuclear spin states of the odd-J molecules (orthohydrogen) are symmetric with respect to particle exchange. The parahydrogen states are therefore nuclear spin singlets (total nuclear spin $I=0$), while the orthohydrogen states are nuclear spin triplets (total nuclear spin $I=1$).[24] The $I=0$ parahydrogen states give no NMR signal. The NMR signal intensity of a thermal equilibrium sample should therefore decrease rapidly below around 50 K, as the hydrogen molecules fall down into the NMR-silent $J=0$ state. However, the experimental results in Fig. 3 show a linear dependence of NMR signal intensity on inverse temperature, in accordance with normal Curie paramagnetism. We may conclude that the samples of H_2@ATOCF are not in thermal equilibrium at low temperature. The NMR signals originate from metastable $J=1$ (orthohydrogen) states, which are prevented from falling down to the $J=0$ (parahydrogen) ground state by the vanishingly small transition probability for this spin-forbidden process. We therefore assume that the observed NMR signals originate purely from trapped $J=1$ orthohydrogen ground states. The other rotational states are neglected in the following discussion.

The $J=1$ state has a rotational degeneracy $g_J=2J+1=3$ in a spherical environment [see Fig. 7(a)]. Distortions from spherical symmetry mean that this rotational symmetry is broken for a H_2 molecule confined in a modified fullerene cage. However, the rotational sublevel splitting is expected to be smaller than the translational splitting, and will be discussed later.

2. Translational quantization

The confinement of the orthohydrogen molecules in the small fullerene cages leads to quantization of the translational degrees of freedom. We treat the translational quantization very approximately by considering the H_2 molecule as a single particle moving freely inside a rigid spherical cavity, i.e., a particle inside an ideal three-dimensional (3D) spherical box. Solution of the Schrödinger equation for this highly simplified case[25] leads to the following translational energy levels:

$$E^{\text{tran}}_{n,\ell} = \frac{\beta^2_{n,\ell}\hbar^2}{2\mu r^2}, \tag{2}$$

where r is the radius of the spherical cavity, μ is the mass of the particle, $n\in\{1,2,\ldots,\}$ is the principal quantum number, $\ell\in\{0,1,\ldots,n-1\}$ specifies the total orbital angular momentum quantum number, and $\beta_{n,\ell}$ is the nth root of the spherical Bessel function $j_\ell(x)$.[26] Translational states with $\ell>0$ possess orbital angular momentum, i.e., the particle executes a circulatory motion inside the cage. The translational degen-

eracy of a level with an orbital quantum number ℓ is $g_\ell = 2\ell + 1$.

This equation predicts a translational ground state $\{n,\ell\}=\{1,0\}$ and a first translational excited state with $\{n,\ell\}=\{1,1\}$, with an energy splitting given by

$$\Delta_{\text{tran}} = \frac{\hbar^2}{2\mu r^2}(\beta_{11}^2 - \beta_{10}^2) = 10.32\frac{\hbar^2}{2\mu r^2}. \tag{3}$$

If the cage is spherical, the translational ground state is threefold degenerate ($g_J=3$ and $g_\ell=1$), while the first translational excited state is nine-fold degenerate ($g_J=3$ and $g_\ell=3$), as shown in Fig. 7(b). The spatial states are labeled $|Jm_Jn\ell m_\ell\rangle$, where $m_J \in \{-J,-J+1,\ldots,+J\}$ and $m_\ell \in \{-\ell,-\ell+1,\ldots,+\ell\}$.

The dimensions of the cavity may be estimated from the crystal structure of ATOCF.[10] The carbon skeleton is roughly ellipsoidal, with principal axes $\{x_C,y_C,z_C\}$, oriented such that the z_C axis points from the cavity center towards the orifice. The ellipsoid diameters are given by $d_x^C \cong 700$ pm, $d_y^C \cong 735$ pm, and $d_z^C \cong 770$ pm in the orifice direction. The translational splitting Δ_{tran} may be estimated from Eq. (3) by setting μ equal to the mass of a hydrogen molecule, and by using an effective spherical box radius given by

$$r \cong \frac{1}{2}d_{\text{rms}} - r_{\text{H}} - r_{\text{C}}, \tag{4}$$

where d_{rms} is the root-mean-square diameter of the carbon skeleton,

$$d_{\text{rms}} = \left\{\frac{1}{3}[(d_x^C)^2 + (d_y^C)^2 + (d_z^C)^2]\right\}^{1/2} \cong 735 \text{ pm}. \tag{5}$$

Here $r_{\text{H}}=120$ pm and $r_{\text{C}}=170$ pm are, respectively, the van der Waals radii of the hydrogen and carbon atoms. This provides an estimated translational splitting of $\Delta_{\text{tran}}/k_B \cong 200$ K. Although this estimate is very rough, it permits us to neglect all but the two lowest translational levels at the temperatures used for the experiments.

The threefold translational degeneracy of the excited state $\{n,\ell\}=\{1,1\}$ is lifted by the broken spherical symmetry of the ATOCF cage. A more realistic energy level diagram is sketched in Fig. 7(c). For simplicity, and because the experimental data are insufficient to characterize a more general interpretation, we assume that translational excited state splits into three equally spaced levels. The splitting is denoted $\epsilon_{\text{tran}}^{11}$. The symmetry-breaking distortion is also expected to quench the orbital angular momentum[27] of the states with $\ell=1$, leading to three real spatial states which represent linear translations along the orthogonal principal axes $\{x_{\text{C}},y_{\text{C}},z_{\text{C}}\}$ of the cavity. The three linearly polarized translational states are denoted $|1m_J11x_{\text{C}}\rangle$, $|1m_J11y_{\text{C}}\rangle$, and $|1m_J11z_{\text{C}}\rangle$ in Fig. 7(c). The quenching of the orbital angular momentum is important since it implies that the spatial orientation of the H_2 molecule is not modulated by the translational motion, even in states with $\ell=1$.

3. Rotational sublevels

In a perfectly spherical environment, the rotation of the H_2 molecule is not associated with an energy change, and the $J=1$ translational ground state $\{n,\ell\}=\{1,0\}$ is threefold degenerate ($g_J=3$). However, in the real case of H_2@ATOCF, each H_2 molecule encounters a nonisotropic environment due to the distorted fullerene cage, thereby breaking the degeneracy.

Assume that the rotational potential may be described approximately by the quadratic form,

$$V(\theta,\phi) = \mathbf{e}_{\text{HH}} \cdot \mathbf{V} \cdot \mathbf{e}_{\text{HH}}, \tag{6}$$

where the unit vector $\mathbf{e}_{\text{HH}}$ is defined to be parallel to the internuclear axis. The principal axes of the symmetric Cartesian tensor $\mathbf{V}$ are denoted $\mathbf{e}_X$, $\mathbf{e}_Y$, and $\mathbf{e}_Z$, with corresponding principal values V_{XX}, V_{YY}, and V_{ZZ}. Although it is not possible to relate this principal axis system to the molecular reference frame *a priori*, one expects the principal axis associated with the lowest principal value to be aligned with the most elongated direction of the distorted icosahedral cage — presumably in the direction of the orifice.

The related problem of H_2 molecules trapped in the interstices of solid C_{60} has been studied closely by Tomaselli.[22] In that case, the S_6 local symmetry of the H_2 environment splits the lowest level into one doubly degenerate level and one nondegenerate state. In the present case of H_2@ATOCF, on the other hand, there is no local symmetry at all, so the $J=1$ rotational state is expected to split into three nondegenerate levels (Fig. 7(d)). The orientation of the H_2 molecule may be defined with respect to the rotational principal axis system using polar angles $\{\theta,\phi\}$, i.e.,

$$\mathbf{e}_{\text{HH}} = \mathbf{e}_Z \cos\theta + \mathbf{e}_X \sin\theta\cos\phi + \mathbf{e}_Y \sin\theta\sin\phi. \tag{7}$$

Since the spatial eigenfunctions must be orthogonal, the spatial wave functions in the $\{n,\ell\}=\{1,0\}$ translational ground state correspond to real p-orbital-like eigenfunctions with angular parts proportional to

$$\begin{aligned} |1Z100\rangle &\propto Y_{10}(\theta,\phi), \\ |1X100\rangle &\propto \tfrac{1}{2}(Y_{11}(\theta,\phi) + Y_{1-1}(\theta,\phi)), \\ |1Y100\rangle &\propto \tfrac{1}{2\text{i}}(Y_{11}(\theta,\phi) - Y_{1-1}(\theta,\phi)), \end{aligned} \tag{8}$$

where $Y_{im}(\theta,\phi)$ are spherical harmonics. One expects the lowest energy level to correspond to a spatial wave function $|1Z100\rangle$ polarized along the most elongated direction of the distorted icosahedral cage—possibly in the direction of the orifice. For simplicity, and because the experimental data are insufficient to characterize a more general interpretation, we assume that the rotational levels of the translational ground state are equally spaced [Fig. 7(d)]. The ground-state rotational sublevel splitting is denoted $\epsilon_{\text{rot}}^{10}$.

A strict analysis of the rotational sublevels would need to take into account the coupling between the translational and rotational degrees of freedom (in a classical description, this coupling corresponds to a change in the orientation of the H_2 molecule on collisions with the cavity wall). For simplicity, we assume that the translational and rotational degrees of freedom may be treated separately.

The excited translational levels are also split. For simplicity, we assume that all sublevels of the $\{n,\ell\}=\{1,1\}$ translational excited state have the same rotational sublevel

splitting, denoted $\epsilon_{\mathrm{rot}}^{11}$. The corresponding spatial states are labeled $|1\mu_J 11\mu_C\rangle$, etc., in Fig. 7(d), where $\mu_J \in \{X,Y,Z\}$ indicates the polarization direction of the rotational state while $\mu_C \in \{x_C, y_C, z_C\}$ indicates the polarization direction of the translational state relative to the cavity. The experimental results are analyzed assuming that $\epsilon_{\mathrm{rot}}^{11}$ and $\epsilon_{\mathrm{rot}}^{10}$ are different.

The complete lifting of the rotational degeneracy in the distorted fullerene cage quenches the rotational angular momentum of the orthohydrogen molecules.[27] This has consequences for the NMR lineshapes (see below).

B. Spin Hamiltonian

As discussed by Tomaselli,[22] the nuclear spin Hamiltonian of the H_2 molecule consists of a through-space dipole-dipole interaction between the two ^{1}H nuclei, as well as a chemical shift anisotropy term. There is also a spin-rotation term, representing the interaction of the nuclear magnetic moments with the rotational angular momentum of the molecule. In hydrogen gas, both of these interactions contribute to the ^{1}H spin-lattice relaxation.[28]

We neglect the spin-rotation interaction in the following discussion. This is justified under the assumption that the broken symmetry of the ATOCF cage quenches the rotational angular momentum of the H_2 molecules in the $J=1$ state, as discussed above. Tomaselli did not observe spectral effects of the spin-rotation interaction, even in the more symmetrical case of H_2 trapped in the interstices between C_{60} molecules.[22]

There is evidence that the chemical shift anisotropy has significant effects on the ^{1}H line shapes, as discussed below.

1. Dipole-dipole coupling

The NMR properties of the endohedral H_2 molecules are dominated by the strong dipole-dipole coupling between the two protons. This interaction is characterized by a dipole-dipole coupling tensor which depends on the rotational/translational state of the molecule. At ordinary temperatures, the H_2 molecules make rapid quantum transitions between the rotational/translational eigenstates, so the NMR spectrum is determined by an average of the dipole-dipole coupling tensor over all of the thermally accessible states, weighted by their fractional populations, according to the Boltzmann distribution.

The nuclear dipole-dipole coupling Hamiltonian in the individual spatial state $|1\mu_J n\ell\mu_C\rangle$ is given by

$$\mathcal{H}_{\mathrm{DD}}^{|1\mu_J n\ell\mu_C\rangle} = \mathbf{I}_1 \cdot \mathbf{D}^{|1\mu_J n\ell\mu_C\rangle} \cdot \mathbf{I}_2, \tag{9}$$

where the two nuclear spins are denoted I_1 and I_2. For simplicity, we assume that the dipole-dipole Hamiltonian is the same in all spatial states $|1\mu_J n\ell\mu_C\rangle$, except for the direction of the dipole-dipole principal axis system, which is given by the polarization direction of the *rotational* state, i.e.,

$$\mathbf{D}^{|1Xn\ell\mu_C\rangle} = b_{\mathrm{DD}}^0 \begin{pmatrix} 2 & 0 & 0 \\ 0 & -1 & 0 \\ 0 & 0 & -1 \end{pmatrix},$$

$$\mathbf{D}^{|1Yn\ell\mu_C\rangle} = b_{\mathrm{DD}}^0 \begin{pmatrix} -1 & 0 & 0 \\ 0 & 2 & 0 \\ 0 & 0 & -1 \end{pmatrix}, \tag{10}$$

$$\mathbf{D}^{|1Zn\ell\mu_C\rangle} = b_{\mathrm{DD}}^0 \begin{pmatrix} -1 & 0 & 0 \\ 0 & -1 & 0 \\ 0 & 0 & 2 \end{pmatrix}.$$

This assumes that the relative orientation of the molecules is independent of the translational motion, which is physically reasonable under the assumption that the orbital angular momentum is quenched by the broken cage symmetry.

The dipole-dipole coupling constant in a linearly polarized $J=1$ rotational state may be estimated through

$$b_{\mathrm{DD}}^0 = -\frac{\mu_0 \gamma^2 \hbar}{4\pi r_{\mathrm{HH}}^3} \frac{2}{5}, \tag{11}$$

where the factor 2/5 takes into account the angular spread of the delocalized nuclear wave functions in the $J=1$ rotational state.[22] The estimated dipole-dipole coupling is $b_{\mathrm{DD}}^0/2\pi \cong -116$ kHz for an internuclear distance $r_{\mathrm{HH}}=74.5$ pm.

At a finite temperature, cage vibrations induce thermal transitions between the translational states. We assume that these transitions are very frequent compared to the size of the nuclear spin interactions, so that the NMR spectrum is determined by the thermally averaged dipole-dipole Hamiltonian, given by

$$\mathcal{H}_{\mathrm{DD}}(T) = \mathbf{I}_1 \cdot \mathbf{D}(T) \cdot \mathbf{I}_2, \tag{12}$$

where

$$\mathbf{D}(T) = \sum_{\mu_J, n, \ell, \mu_C} \mathbf{D}^{|1\mu Jn\ell\mu C\rangle} p^{|1\mu Jn\ell\mu C\rangle}(T). \tag{13}$$

Here $p^{|1\mu_J n\ell\mu_C\rangle}(T)$ is the fractional thermal occupancy of an individual spatial state, as determined by the Boltzmann distribution at the temperature T, i.e.,

$$p^{|1\mu_J n\ell\mu_C\rangle}(T) = Z^{-1}(T) \exp - E^{|1\mu_J n\ell\mu_C\rangle}/k_B T, \tag{14}$$

where the partition function is

$$Z(T) = \sum_{\mu_J, n, \ell, \mu_C} \exp - E^{|1\mu_J n\ell\mu_C\rangle}/k_B T. \tag{15}$$

The thermally averaged dipolar Hamiltonian can therefore be written as a tensor of the form

$$\mathbf{D}(T) = \begin{pmatrix} D_X(T) & 0 & 0 \\ 0 & D_Y(T) & 0 \\ 0 & 0 & D_Z(T) \end{pmatrix}, \tag{16}$$

where the principal axes correspond to the principal axes of the rotational potential, and the principal values are given by

$$D_X(T) = b_{DD}^0 Z^{-1} \sum_{n,\ell,\mu_C} (2p^{|1Xn\ell\mu_C\rangle} - p^{|1Yn\ell\mu_C\rangle} - p^{|1Zn\ell\mu_C\rangle}),$$

$$D_Y(T) = b_{DD}^0 Z^{-1} \sum_{n,\ell,\mu_C} (-p^{|1Xn\ell\mu_C\rangle} + 2p^{|1Yn\ell\mu_C\rangle} - p^{|1Zn\ell\mu_C\rangle}),$$

$$D_Z(T) = b_{DD}^0 Z^{-1} \sum_{n,\ell,\mu_C} (-p^{|1Xn\ell\mu_C\rangle} - p^{|1Yn\ell\mu_C\rangle} + 2p^{|1Zn\ell\mu_C\rangle}). \quad (17)$$

The thermally averaged dipole-dipole coupling constant $b_{DD}(T)$ and dipolar biaxiality (asymmetry) parameter $\eta_{DD}(T)$ are given by

$$b_{DD}(T) = D_z(T), \quad \eta_{DD}(T) = \frac{|D_Y(T) - D_X(T)|}{|D_Z(T)|}. \quad (18)$$

At the lowest temperature, only the lowest sublevel is populated, and the dipole-dipole (DD) coupling tensor is expected to have zero biaxiality, with a coupling constant $b_{DD}(T\to 0)/2\pi = b_{DD}^0/2\pi \cong -116$ kHz. As the temperature is increased, the neighboring levels are populated, the DD coupling constant decreases in magnitude, and the biaxiality increases. At high temperatures, the DD coupling constant becomes small, since the populations of states which are polarized in the three orthogonal spatial directions become nearly equal. The dashed lines in Fig. 8 show a typical trajectory for the dipole-dipole coupling parameters as a function of temperature.

The treatment given above predicts that the principal axis system $\{X, Y, Z\}$ of the DD coupling tensor remains fixed in the molecular reference frame, even though the DD coupling constant and the biaxiality are both strongly temperature dependent. Unfortunately, this result cannot be tested at the present time, since single crystals of H_2@ATOCF are not available.

2. Chemical shift interactions

The proton nuclei also experience chemical shifts from the electrons in the surrounding fullerene cage and the hydrogen molecule itself. This interaction may be described by a Hamiltonian term of the form

$$\mathcal{H}_{CS}(T) = \mathbf{B}^0 \cdot \boldsymbol{\delta}(T) \cdot (\mathbf{I}_1 + \mathbf{I}_2), \quad (19)$$

where $\mathbf{B}^0$ is the external magnetic field and $\boldsymbol{\delta}$ is the chemical shift tensor (defined using the deshielding convention). In principle the chemical shift tensor depends on the spatial rotational state of the H_2 molecule, and hence on temperature. However, if the electronic shielding is dominated by the effect of the distorted fullerene cage, which seems reasonable, the chemical shift tensor may be assumed to be temperature independent.

In the following discussion, we assume a temperature-independent shielding tensor, dominated by the influence of the cage. This simplified model is sufficient to treat the experimental results.

3. Secular spin Hamiltonian

In high magnetic field, the Hamiltonians in Eqs. (12) and (19) are truncated against the dominant Zeeman interaction with the main magnetic field (secular approximation). The high-field spin Hamiltonian is therefore approximated by

$$\mathcal{H} = \mathcal{H}_{DD} + \mathcal{H}_{CS}, \quad (20)$$

with

$$\mathcal{H}_{DD} \cong \sum_{m=-2}^{+2} A_{2m}^{DD} D_{m0}^2(\Omega_{PL}^{DD}) T_{20}, \quad (21)$$

and

$$\mathcal{H}_{CS} \cong \left\{ \delta^{iso} B^0 + \sum_{m=-2}^{+2} A_{2m}^{CSA} D_{m0}^2(\Omega_{PL}^{CSA}) \right\} T_{10}, \quad (22)$$

where the spherical tensor spin operator components are

$$T_{10} = I_{1z} + I_{2z}, \quad T_{20} = \frac{1}{\sqrt{6}}(3I_{1z}I_{2z} - \mathbf{I}_1 \cdot \mathbf{I}_2). \quad (23)$$

The spherical tensor representation of the spatial part of the DD coupling, written in its own principal axis frame, is given by

$$A_{20}^{DD} = \sqrt{6} b_{DD}, \quad A_{2\pm1}^{DD} = 0, \quad A_{2\pm2}^{DD} = -\eta_{DD} b_{DD}, \quad (24)$$

where $\Omega_{PL}^{DD} = \{\alpha_{PL}^{DD}, \beta_{PL}^{DD}, \gamma_{PL}^{DD}\}$ are the Euler angles relating the principal axis system of the rotational potential to the laboratory frame, whose z axis is along the applied magnetic field. Similarly, the spatial part of the chemical shift anisotropy (CSA) tensor, written in its own principal axis frame, is given by

$$A_{20}^{CSA} = B^0 \delta^{CSA}, \quad A_{2\pm1}^{CSA} = 0, \quad A_{2\pm2}^{CSA} = -\frac{1}{\sqrt{6}} B^0 \eta^{CSA} \delta^{CSA}, \quad (25)$$

where $\Omega_{PL}^{CSA} = \{\alpha_{PL}^{CSA}, \beta_{PL}^{CSA}, \gamma_{PL}^{CSA}\}$ are the Euler angles relating the principal axis system of the chemical shift anisotropy tensor to the laboratory frame. Here δ^{CSA} is the magnitude of the chemical shift anisotropy (defined as the largest displacement of a chemical shift principal value from the isotropic shift), and η^{CSA} is the biaxiality of the chemical shift anisotropy.

The secular Hamiltonian in Eq. (20) may be used for line shape and spinning-sideband calculations using standard methods.[29]

C. Line shapes

1. Static ^{1}H line shapes

At low temperatures, the secular Hamiltonian is dominated by the dipole-dipole term in Eq. (21). This gives rise to a broad spectral line shape with a maximum width of $3b_{DD}$. The line shape has the form of a Pake pattern for the uniaxial case $\eta_{DD}=0$ but acquires a different shapes for finite biaxiality.

The static experimental line shape at 4.3 K, shown in Fig. 2, has the form of a uniaxial Pake pattern with maximum width ~350 kHz. This closely resembles the spectrum for the dipole-dipole coupling parameters

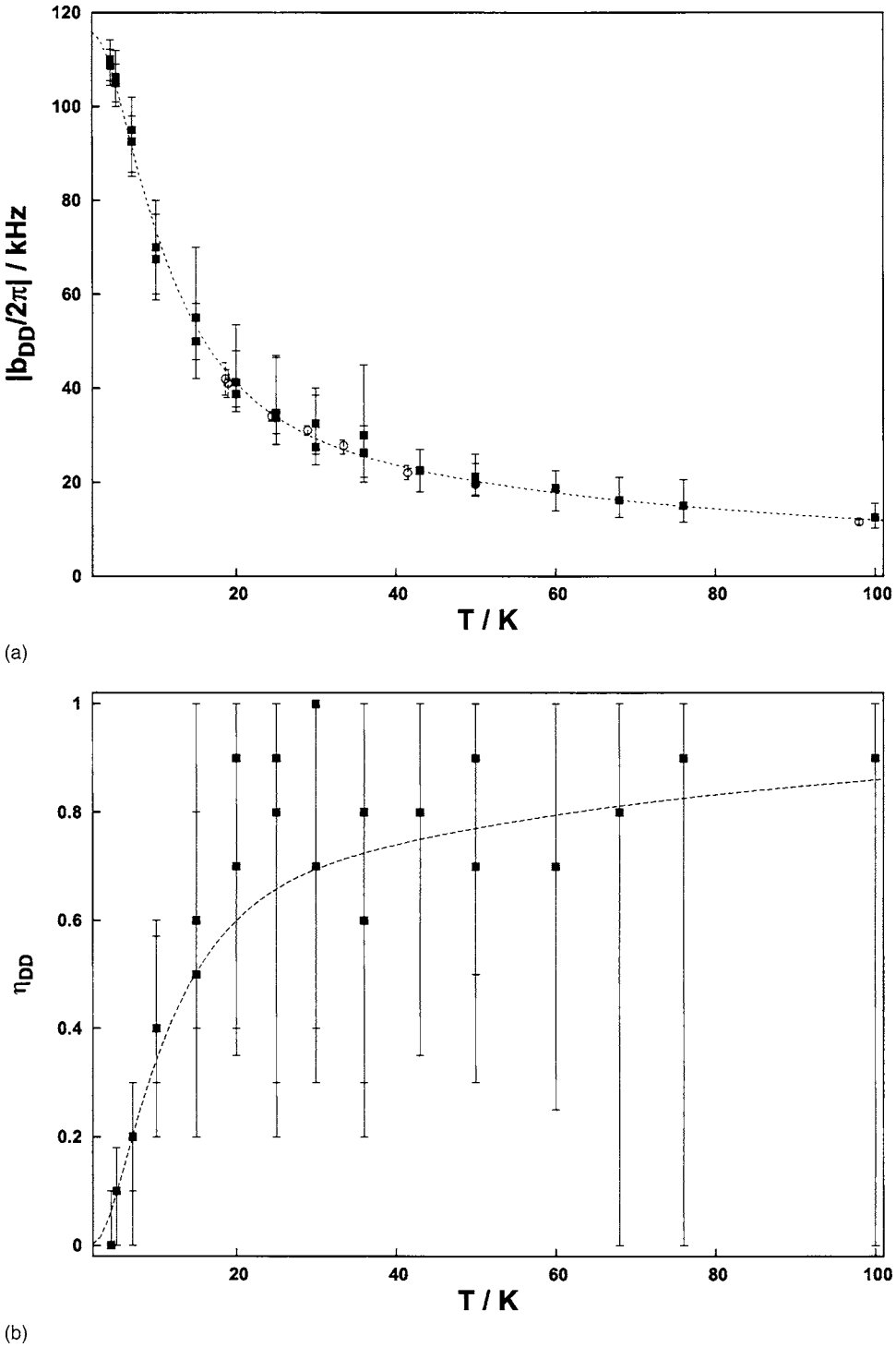

FIG. 8. (a) Dipole-dipole coupling constant $|b_{DD}/2\pi|$ and confidence limits as a function of temperature for H_2@ATOCF, determined from the static ^{1}H spectra (squares) and the MAS spectra (circles). (b) Dipole-dipole biaxiality η_{DD} and confidence limits as a function of temperature for H_2@ATOCF, determined from the static ^{1}H spectra (squares). The dashed lines are the best theoretical fits, using $\Delta_{tran}/k_B=113.0\pm11.0$ K, $\epsilon_{rot}^{10}/k_B=13.6\pm0.5$ K, and $\epsilon_{rot}^{11}/k_B=26.0\pm3.5$ K while imposing $\epsilon_{tran}^{11}/k_B=0$ K.

$|b_{DD}/2\pi| \cong 116$ kHz and η_{DD} predicted by Eq. (18), assuming that the single rotational-translational state $|1Z11z_C\rangle$ is populated. The 4.3 K spectrum in Fig. 2 therefore represents the NMR spectra of H_2 molecules prepared in a pure spatial quantum state.

The DD coupling parameters b_{DD} and η_{DD} were estimated as a function of temperature by fitting the spectra in Fig. 2 to the results of two-spin simulations. To improve the accuracy of the fit a small Gaussian component was added to the simulated spectra, offset by $\sim+12$ ppm, in order to take into account the unsuppressed exohedral signal.

Analysis of the MAS data (see below) provided an estimate of the chemical shift anisotropy of the order of $\delta^{CSA}=8.33$ ppm. We verified that a chemical shift anisotropy of this size has a negligible effect on the static ^{1}H line shapes. The CSA was omitted from the simulations shown in Fig. 2.

The dashed lines in Fig. 2 show the results of these fits. In order to estimate the confidence limits of the dipole coupling parameters, static powder line shapes were computed over a grid of b_{DD} and η_{DD} values. A χ^2 surface was computed at each temperature by calculating the root-sum-square deviation between experiment and simulation. For each temperature, the confidence region for the dipolar parameters was estimated from the extremes of the $\chi^2=1.2\chi_g^2$ contour,

where χ_g^2 is the global minimum in χ^2 over the $\{b_{DD}, \eta_{DD}\}$ space.[30] These confidence intervals are shown for each temperature in Fig. 8. At the lowest temperatures, the dipole-dipole coupling constant and the dipolar biaxiality are both well defined, but at the higher temperatures, the biaxiality η_{DD} is indeterminate.

The energy splittings Δ_{tran}, ϵ_{tran}^{11}, ϵ_{rot}^{10}, and ϵ_{rot}^{11} were estimated by fitting the theoretical DD coupling parameters [Eqs. (17) and (18)] to the experimental temperature dependence shown in Fig. 8. Satisfactory fits were obtained using the following values: $\Delta_{tran}/k_B = 113 \pm 11$ K, $\epsilon_{rot}^{10}/k_B = 13.6 \pm 0.5$ K, and $\epsilon_{rot}^{11}/k_B = 26 \pm 3$ K. The fit is very insensitive to the parameter ϵ_{tran}^{11} for values up to a few hundreds kelvin, which has therefore been set to zero. The theoretical temperature dependence of the DD coupling parameters associated with these energy splittings is shown as dashed lines in Fig. 8.

These energy level splittings are physically reasonable. In particular, the $\Delta_{tran}/k_B \cong 113$ K translational splitting is of the same order of magnitude as the particle-in-a-box estimate (see above). Even the result that ϵ_{rot}^{11} is larger than ϵ_{rot}^{10} may be rationalized by noting that the excited translational state explores regions closer to the walls of the box, where the rotational potential is expected to be strong.

Slightly different estimates for the spatial energy level splittings could be obtained by lifting the constraint that the rotational splittings are equal. We did not explore more sophisticated models in detail since they did not lead to significantly improved fits.

2. Magic-angle-spinning sideband patterns

The secular Hamiltonian in Eq. (21) may be used to calculate powder spinning sideband amplitudes, using standard methods.[29] The dipolar coupling parameters $\{b_{DD}, \eta_{DD}\}$ may therefore be estimated by comparing simulated MAS sideband amplitudes with the experimental sideband intensities.

In order to extract the sideband amplitudes of the endohedral H_2 signals in Fig. 4(a) we subtracted a model of the broad exohedral signal, assuming that it is approximately linear in the region of each narrow sideband. Figure 4(b) shows the experimental sideband amplitudes of the endohedral H_2 molecules, extracted by this procedure. The lack of symmetry in the sideband amplitudes indicates the presence of a sizeable CSA interaction.

Simulated sideband intensities, adjusting b_{DD} and η_{DD} for a best fit to the experimental data at each temperature, are shown in Fig. 4(c). The same CSA tensor was used at all temperatures. The CSA parameters used in the simulations are $\delta^{CSA} = 8.33$ ppm and $\eta^{CSA} = 0$. The CSA tensor has the same orientation as the DD tensor.

The magnitude of the CSA was estimated to be $\delta^{CSA} = 8.3 \pm 2.8$ ppm, and is temperature independent within experimental error. The biaxiality was estimated to be $\eta^{CSA} < 0.2$. It was not possible to estimate the orientation of the CSA tensor with respect to the DD coupling tensor. The temperature independence of the CSA is consistent with a mechanism in which the CSA is dominated by electronic shielding from the fullerene cage.

The temperature dependence of b_{DD}. as determined from the MAS spinning sidebands, are shown in Fig. 8(a). The confidence limits on the b_{DD} values are also shown. We do not report the temperature dependence of η_{DD}, as determined from the MAS spinning sidebands, since the confidence limits on η_{DD} were found to be very wide at most temperatures.

Figure 8(a) shows that there is a good level of agreement between the DD coupling values determined by static ^{1}H spectroscopy and by MAS experiments over the entire temperature range. Since the sample temperature is controlled very well in static NMR experiments, this good correspondence indicates that the true sample temperature in the MAS experiments must be close to the readout of the exit gas temperature. We conclude that there is no evidence of any measurable sample heating as a result of the sample rotation at cryogenic temperatures, within the accuracy of our measurements.

D. Spin relaxation

The spin-lattice relaxation of endohedral H_2 molecules is expected to be dominated by the thermally driven reorientation of the DD coupling tensor as transitions are made between the spatial quantum states in Fig. 7. Since a complete relaxation theory does not yet exist for this complicated case, we have attempted to treat the T_1 process by the two-site Look-Lowe model.[31] In this case the DD coupling executes stochastic jumps between two sites with different principal axis orientations and different energies. This resembles the situation at the lowest temperatures studied here, where the H_2 molecules explore the two lowest spatial eigenstates $|1Z11z_C\rangle$ and $|1Y11z_C\rangle$, in which the DD coupling tensors are at 90° to each other. However, since the line shape analysis gave an estimated rotational splitting $\epsilon_{rot}^{10}/k_B = 13.7 \pm 0.5$ K, the Look-Lowe model is only expected to apply at temperatures below around 15 K. At higher temperatures, many more spatial states become active and the Look-Lowe model is expected to break down.

The Look-Lowe expression for the relaxation rate constant of the endohedral H_2 molecules is

$$T_{1,endo}^{-1} = c_{LL}\,\mathrm{sech}^2\left(\frac{\Delta E_{LL}}{2k_BT}\right), \tag{26}$$

where c_{LL} contains all field and geometry information and ΔE_{LL} is the energy splitting between the two levels under consideration.

We must also remember that the samples studied here contain an excess of endohedral protons, which are presumably immobile in the cryogenic regime, and whose main relaxation mechanism is cross relaxation with the endohedral H_2 molecules, which act as a relaxation sink. The observed relaxation rates are therefore weighted averages of the endohedral proton relaxation rate constants and the very low rate constants of the immobile exohedral protons. A Look-Lowe interpretation of the relaxation data should therefore be based on

$$T_1^{-1} \cong cT_{1,endo}^{-1}, \tag{27}$$

where

$$c = \frac{N_{\text{endo}}}{N_{\text{exo}} + N_{\text{endo}}}. \tag{28}$$

Here, N_{endo} and N_{exo} are the numbers of endohedral/exohedral protons in the material and $T_{1,\text{exo}}^{-1}$ is assumed to be neglibly small. In a pure sample of H_2@ATOCF, the ratio $N_{\text{exo}}:N_{\text{endo}}$ is 8:1. In practice, the ratio is somewhat higher than this, since the encapsulation yield is may be somewhat less than 100% and only about 75% of H_2 molecules are expected to be in the ortho state.

This relaxation sink model is supported by the magic-angle-spinning relaxation data (Fig. 5), where the endohedral relaxation rates were found to be much faster in the presence of magic-angle spinning, compared to those measured in a static sample. The fast magic-angle spinning averages out the endo-exo DD interactions, which drive cross relaxation in a static sample, and thereby isolates the two reservoirs. This effect has also been seen clearly at high temperatures.[11]

Equation (27) may be fitted to the cryogenic region of the T_1 vs T^{-1} curves, as shown in Fig. 6 (solid and dashed lines). The fit parameters are $c_{\text{LL}}=5.7\pm0.3\ \text{s}^{-1}$ and $\Delta E_{\text{LL}}/k_B=18.8\pm0.7$ K at a field of 0.735 T, and $c_{\text{LL}}=1.3\pm0.2\ \text{s}^{-1}$ and $\Delta E_{\text{LL}}/k_B=18.6\pm2.1$ K at a field of 8.46 T. The Look-Lowe energy gap ΔE_{LL} is consistent at the two magnetic fields, but the Look-Lowe constant c_{LL} differs by a factor of around 4 at the two magnetic fields. This may be due in part to sampling of the spectral density at two very different Larmor frequencies. However, at the moment, we have not been successful with a more detailed interpretation of these results in a quantitative analysis using a single correlation time.

The Look-Lowe model clearly fails, as anticipated, at temperatures higher than the rotational energy gap of around 15 K. At higher temperatures, the Look-Lowe two-site model greatly underestimates the relaxation rates, indicating that more than two spatial states become active in the relaxation process at higher temperatures. This observation is consistent with the energy level structure in Fig. 7. A more sophisticated relaxation treatment is under preparation.

V. CONCLUSIONS

The endohedral complexes of H_2 with fullerenes and their derivatives provide a robust and versatile series of systems for studying the quantum mechanics of confined molecules by NMR. In contrast to exohedral H_2-fullerene complexes,[22] the endohedral species are stable under ordinary conditions without the need for a hydrogen atmosphere. This allows magic-angle spinning, which provides high sensitivity and resolution, and permits the study of cryogenic phenomena by NMR with chemical site selectivity. Other isotopomers such as D_2 and HD may be inserted into the cages, allowing the study of different rotational quantum states.[22] In some systems, it is even possible to insert several He atoms into the cages,[2] providing the unusual prospect of studying ^{3}He–^{3}He dipole-dipole couplings.

The environment of the confined molecules may be modified by changing the substituents attached to the cage. Recently, endohedral complexes of H_2 within complete C_{60} cages have been prepared by resealing the orifices after insertion of hydrogen.[8] These complexes provide an icosahedral local environment for the endohedral H_2 molecules, which should lead to a degenerate (or a nearly degenerate) spatial ground state. Unusual cryogenic relaxation and line shape effects are anticipated. This substance is now under study in our laboratory.

The relaxation data shown in Fig. 5 and in Ref. 11 show that the endohedral protons act as relaxation sinks for protons outside the cage. This suggests the possibility of using endohedral H_2@C_{60} complexes as diamagnetic relaxation agents for NMR at low temperatures. NMR signals are stronger at low temperatures since the nuclear spin polarization is proportional to T^{-1}. The high signal strength of cryogenic NMR holds great promise for studies of materials and biomolecules, where the applications of NMR are currently limited by the relatively poor sensitivity of the method. However, the potential sensitivity advantage of the cryogenic regime can be difficult to exploit since spin-lattice relaxation becomes very slow for many materials at low temperatures. This problem could be overcome by complexing cryorelaxation agents such as H_2@C_{60} with the material of interest, providing a relaxation sink for the surrounding molecular environment. In many cases the relaxation enhancement will be more specific and nonperturbing than that provided by paramagnetic relaxation agents. In some cases, no chemical modifications of the relaxation agents will be necessary. For example, C_{60} binds strongly with the hydrophobic pocket of HIV protease.[32]

ACKNOWLEDGMENTS

This research was supported by the Basic Technology program (UK), EPSRC (UK), and the Estonian Science Foundation. One of the authors (M.C.) would like to thank Jacco van Beek for making the MATNMR software package[33] freely available.

[1] M. Saunders, R. J. Cross, H. A. Jiménez-Vázquez, R. Shimshi, and A. Khong, Science **271**, 1693 (1996).
[2] D. E. Giblin, M. L. Gross, M. Saunders, H. A. Jiménez-Vázquez, and R. J. Cross, J. Am. Chem. Soc. **119**, 9883 (1997).
[3] T. A. Murphy, T. Pawlik, A. Weidinger, M. Hohne, R. Alcala, and J. M. Spaeth, Phys. Rev. Lett. **77**, 1075 (1996).
[4] A. Weidinger, M. Waiblinger, B. Pietzak, and T. A. Murphy, Appl. Phys. A: Mater. Sci. Process. **66**, 287 (1998).
[5] R. J. Cross, A. Khong, and M. Saunders, J. Org. Chem. **68**, 8281 (2005).
[6] Y. Rubin, T. Jarrosson, G.-W. Wang, M. D. Bartberger, K. N. Houk, G. Schick, M. Saunders, and R. J. Cross, Angew. Chem., Int. Ed. **40**, 1543 (2001).
[7] Y. Murata, M. Murata, and K. Komatsu, J. Am. Chem. Soc. **125**, 7152 (2003).
[8] K. Komatsu, M. Murata, and Y. Murata, Science **307**, 238 (2005).
[9] S. Iwamatsu, S. Murata, Y. Andoh, M. Minoura, K. Kobayashi, N. Mizorogi, and S. Nagase, J. Org. Chem. **70**, 4820 (2005).
[10] Y. Murata, M. Murata, and K. Komatsu, Chem.-Eur. J. **9**, 1600 (2003).
[11] Y. Carravetta, Y. Murata, M. Murata, I. Heinmaa, R. Stern, A. Tontcheva, A. Samoson, Y. Rubin, K. Komatsuand, and M. H. Levitt, J. Am. Chem. Soc. **126**, 4092 (2004).
[12] I. J. Lowe, Phys. Rev. Lett. **2**, 285 (1959).
[13] E. R. Andrew, A. Bradbury, and R. G. Eades, Nature (London) **183**, 1802 (1959).
[14] A. Hackmann, H. Seidel, R. D. Kendrick, P. C. Myhre, and C. S. Yannoni, J. Magn. Reson. (1969-1992) **79**, 148 (1988).
[15] P. C. Myhre, G. G. Webb, and C. S. Yannoni, J. Am. Chem. Soc. **112**, 8991 (1990).

[16] A. Samoson, T. Tuherm, J. Past, A. Reinhold, T. Anupöld, and I. Heinmaa, Top. Curr. Chem. **246**, 15 (2004).
[17] A. J. Horsewill and Q. Xue, Phys. Chem. Chem. Phys. **4**, 5475 (2002).
[18] M. Shiraishi and M. Ata, J. Nanosci. Nanotechnol. **2**, 463 (2002).
[19] T. N. Su, S. L. Chen, P. C. Taylor, R. S. Crandall, and A. H. Mahan, Phys. Rev. B **62**, 12849 (2000).
[20] T. N. Su, P. C. Taylor, S. L. Chen, R. S. Crandall, and A. H. Mahan, J. Non-Cryst. Solids **266**, 195 (2000).
[21] N. S. Sullivan, M. Rall, and J. P. Brison, J. Low Temp. Phys. **98**, 383 (1995).
[22] P. M. Tomaselli, Mol. Phys. **101**, 3029 (2003).
[23] P. M. Rafailov, C. Thomsen, A. Bassil, K. Komatsu, and W. Bacsa, Phys. Status Solidi B **242**, R106 (2005).
[24] J. Natterer and J. Bargon, Prog. Nucl. Magn. Reson. Spectrosc. **31**, 293 (1997).
[25] P. F. Newhouse and K. C. McGill, J. Chem. Educ. **81**, 424 (2004).
[26] M. Abramowitz and I. A. Stegun, *Handbook of Mathematical Functions* (Dover, New York, 1970).
[27] C. P. Slichter, *Principles of Magnetic Resonance* (Springer-Verlag, Berlin, 1992).
[28] A. Abragam, *The Principles of Nuclear Magnetism* (Clarendon, Oxford, 1961).
[29] S. A. Smith, T. O. Levante, B. H. Meier, and R. R. Ernst, J. Magn. Reson., Ser. A **106**, 75 (1994).
[30] W. H. Press, B. P. Flannery, S. A. Teukolsky, and W. T. Vetterling, *Numerical Recipes in C* (Cambridge University Press, Cambridge, UK, 1986).
[31] D. C. Look and I. J. Lowe, J. Chem. Phys. **44**, 2995 (1966).
[32] S. H. Friedman, D. L. DeCamp, R. P. Sijbesma, G. Srdanov, F. Wudl, and G. L. Kenyon, J. Am. Chem. Soc. **115**, 6506 (1993).
[33] MATNMR is a toolbox for processing NMR/EPR data under MATLAB and can be freely downloaded at http://matnmr.sourceforge.net, 2005.